Full length article

Prediction of transformation stresses in NiTi shape memory alloy

S. Alkan [a], H. Sehitoglu [b], *

[a] Department of Mechanical Engineering, Bogazici University, Bebek, Istanbul, 34342, Turkey
[b] Department of Mechanical Science and Engineering, University of Illinois at Urbana-Champaign, 1206 W. Green Street, Urbana, IL, 61801, USA

ABSTRACT

It is well known that interfaces play an important role in determining the mechanical response of materials. This paper focuses on the transforming shape memory alloy NiTi and is aimed towards a better understanding of austenite-martensite interface structure (steps and dislocation arrays) and the determination of transformation stress corresponding to the translation of this interface. In the present work, we characterize the defect content at the cubic-monoclinic interfaces via the Topological Model. The defect-induced displacement fields are generated within the framework of the Eshelby-Stroh formalism and further improved with Molecular Statics simulations accounting for interactions at the atomic level. The resulting defect core disregistry fields are employed as input to a modified Peierls-Nabarro framework for evaluating the transformation stress. We applied the proposed methodology to the particular case of NiTi alloy single crystals of specific orientations and predicted the transformation stress levels in close agreement with experiments. Moreover, the short-range interactions of dislocation core disregistry fields are shown to be responsible for the experimentally observed non-Schmid behavior of transformation stress levels. Overall, the paper represents an effort to improve our understanding of shape memory materials considering theory, computer simulation and experiment.

© 2019 Acta Materialia Inc. Published by Elsevier Ltd. All rights reserved.

1. Introduction

The focus of this paper is on understanding the theoretical origins of the non-Schmid behavior in a shape memory alloy reflected by the deviation of CRSS (Critical Resolved Shear Stress), i.e. the lattice resistance against the glide of phase transformation front, from constant critical resolved shear stress rule. To this end, we chose equiatomic NiTi which is the most successful and well-known shape memory alloy. In early studies, we explained the non-Schmid plastic flow behavior of shape memory alloys [1–5] based on the coupling between the applied loading direction and the non-planar dislocation core structure. By a similar analogy, the core structures of the interfacial dislocations formed at the transformation front is expected to play a key role in the anisotropic character of CRSS levels observed in the earlier experimental works [6–8]. The non-Schmid behavior of interfacial dislocation cores can have two main consequences for NiTi: (i) the variation of the CRSS as a function of the stress state as demonstrated in tension-compression asymmetry and crystal orientation effects [3], and (ii) it can lead to discrepancies between the favored variants in the

experiments and the predicted ones relying on the Schmid Law. This type of a deviation from Schmid Law has been demonstrated in NiTi [9]. Despite its importance, no comprehensive theory has been developed on non-Schmid behavior of athermal transformation CRSS levels as addressed in this study. The main goal of this work is to establish a theoretical framework for determining athermal CRSS levels in transforming materials employing the crystallographic interface structure.

Understanding the interfaces in metals has been a major goal in bridging microstructure and mechanical response [10–17]. The efforts for quantifying the mechanical response of interfaces inevitably results in visiting the concept of dislocations and disconnections (dual step/dislocation character defects) [18–20] the presence of which has been evidenced by the accompanying Transmission Electron Microscopy (TEM) studies [21,22]. On theoretical grounds, a number of frameworks have been proposed to predict these defect arrays based on the lattice parameters and orientations of the neighboring crystals [23–25]. Distinct from the other methodologies, the TM developed by Pond et al. [26–28] allows one to embrace the discrete lattice structure generated at

* Corresponding author.
E-mail address: huseyin@illinois.edu (H. Sehitoglu).

the interface employing crystal symmetry operations and is capable of predicting not only the Burgers vector density but also the surface step density.

The earlier investigations on transforming alloys [29–38] also point to the fact that the defect content of austenite-martensite transformation front can play a significant role on mechanical behavior. Despite its importance, a theoretical methodology incorporating atomic interactions for predicting the transformation stress is yet to be established. Specifically, in this work, the equiatomic NiTi austenite-martensite habit plane and Type II-1 martensitic twin boundary structures are established via the Topological Model (TM) [26,39,40]. Subsequent to determination of the associated displacement and stress fields via the anisotropic elasticity (Stroh) formulation [41], the modified Peierls-Nabarro framework is implemented [2,31] for theoretical CRSS value calculations. In summary, the purpose of this work is to advance the modeling of the interface motion in the presence of a defect network without *a priori* assumptions and empirical constants. The work extends previous treatments by developing a novel methodology to predict the transformation CRSS levels. Ultimately, we predict the non-Schmid behavior of transformation stress levels associated with the austenite-martensite interface motion in NiTi shape memory alloys yielding very close agreement with the experimental measurements.

The paper is organized as follows: in section 2.1, we summarize the general methodology in capsule form. Subsequently, in section 2.2, we provide the topological model and establish the misfit strains, the defect structure and the habit plane. In section 2.3, the displacement fields are determined and then modified by including relaxation effects by molecular statics, and in Section 2.4 the anisotropic CRSS levels are determined utilizing an energy formulation. In section 3 and 4, we provide the simulation results and discussion of the findings respectively. Finally, in section 5 we end with conclusions. The nomenclature employed in the present work is provided in Appendix A.

2. Theoretical modeling

2.1. General framework

The individual steps followed through the solution methodology are summarized in Fig. 1. In Fig. 1, b^D refers to the Burgers vector of disconnection which also has a step character and accommodates a portion of the misfit strain. On the other hand, the b^{LIS} stands for the dislocation Burgers vector formed as a result of the remnant portion of the interface misfit strain which cannot be solely accommodated by the disconnections. Meanwhile, in general b^{LIS} can be either associated with slip or twinning, in the particular case of equiatomic NiTi, it corresponds to Type II-1 twinning dislocations. Throughout the interface characterization strategy adopted in the present work, firstly, the atomic registry on the terrace plane of {110} [31] family is constructed by bringing the B2 and B19' lattices of austenite and martensite phases of NiTi into coincidence [42]. At this step, the origin is chosen as the neutral lattice point at which Ni atoms on both phases are coincident. Following the geometric characterization of this reference configuration; the corresponding misfit strain, step height, the Burgers vectors and the spatial frequencies of the disconnections and Type II -1 twinning dislocations are calculated along with the accompanying rigid body rotation. Furthermore, an iterative convergent calculation scheme initially proposed by Pond et al. [28] has been employed to evaluate the habit plane indices from the reference {110} terrace plane. Following the determination of the habit plane and its pertinent defect content by the TM, the atom occupation sites under interatomic force field are determined by the relaxation calculations within the framework of MS simulations employing Large-scale Atomic/Molecular Massively Parallel Simulator (LAMMPS) [43]. The interatomic force field is generated based on the NiTi potential developed in our group [44] which can capture the elastic stiffness tensor components in close agreement with the experimental measurements in both austenite and martensite
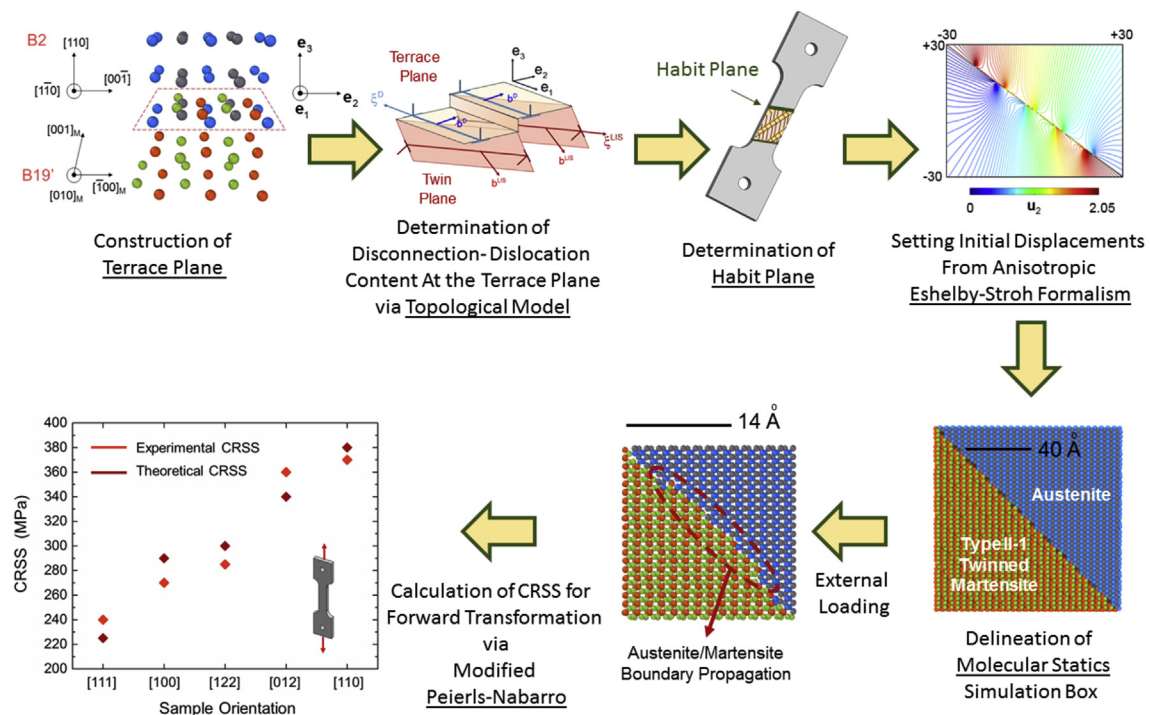

Fig. 1. Summarizes the steps taken throughout calculations in the present study to predict the forward transformation CRSS with the employed computational models and tools underlined.
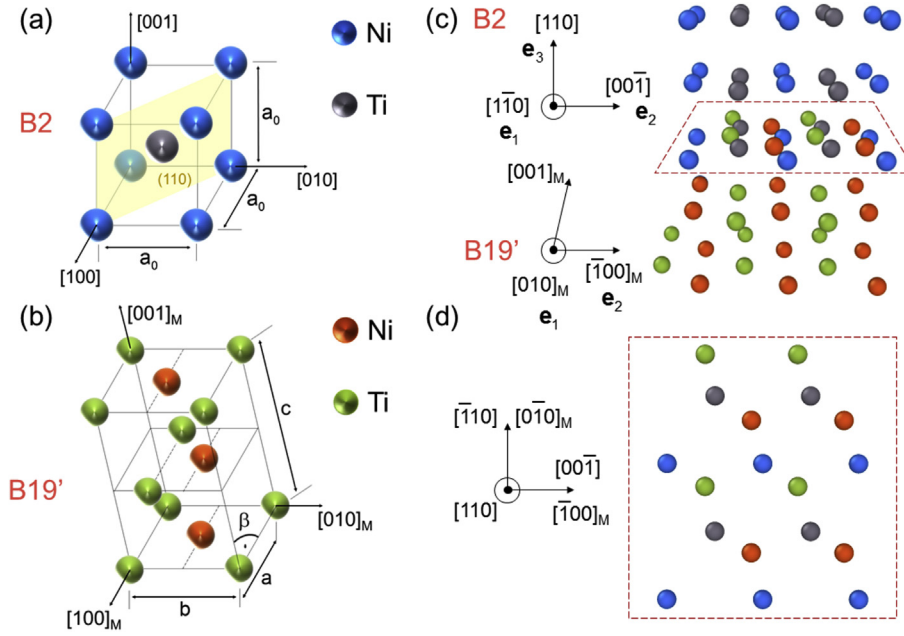
Fig. 2. (a) Shows the B2 ordered austenite lattice structure in equiatomic NiTi. **(b)**shows the monoclinic lattice structure (excluding shuffle motion of atoms) in equiatomic NiTi. The dashed lines correspond to b/2 and b/3 spacings. **(c)** demonstrates the crystallographic orientation of the disconnection along with the step formation on the terrace plane indicated by the dashed plane. **(d)**The planar view of the atomic configurations on the unrelaxed terrace plane is presented.

phases. The displacement field associated with the Burgers vectors of the disconnections and the twinning dislocations are embodied within the framework of anisotropic elasticity following the seminal works of Bonnet et al. and Lothe et al. [45,46] based upon Eshelby-Stroh formalism [41,47]. The relaxation calculations are conducted in a simulation cell of $120 \times 120 \times 9 \, \text{Å}^3$ in both externally-stress free and under uniaxial tensionalong [100, 110, 111, 122] and [012] crystallographic directions. These atomic scale calculations allow us to capture disregistry fields inside the defect cores and the CRSS levels which are associated with the transformation front glide initiation.

In order to calculate the transformation CRSS levels in a precise fashion, we invoked the modified Peierls-Nabarro framework which is shown to yield successful predictions for the CRSS levels in the earlier studies for slip [1,2,31,48]. This approach employs the total energy functional embracing both long range elastic energy associated with the interface defect array and the short range lattice transformation, generalized planar and stacking fault energies comprising the Type II-1 twinning as well as the misfit energy barriers respectively. The resulting CRSS value corresponds to the maximum gradient of the total energy functional with respect to the corresponding disregistry fields. In the following subsection, we will focus on the first step, i.e. construction of the terrace plane from the crystallography of B2 and B19' crystal structures via the TM in a quantitative fashion.

2.2. Topological model and crystallography of habit plane in NiTi

The crystal structures of austenite (B2 structure-$Pm\overline{3}m$space group) and martensite (B19' structure-P21/m space group) phases are shown in Fig. 2(a) and (b) respectively along with the corresponding lattice constants which are tabulated in Table 1 [49]. As a first attempt to calculate the indices of habit plane of semi-coherent structure via the TM, we employed the crystallographic orientation relationships derived based on TEM imaging studies conducted on NiTi which suggest correspondence between the $(110)||(001)_M$ planes with an angular difference of 6.5° and

Table 1
The lattice constants of austenite, a_0, and the monoclinic martensite, a, b, c, β phases are tabulated [49].

a_0 (Angstroms)	a (Angstroms)	b (Angstroms)	c (Angstroms)	β (Degrees)
3.015	2.889	4.120	4.622	96.3°

the$[110]||[010]_M$ directions within a range of 2° to 4° [50]. The terrace plane constructed based upon these orientation relations is visualized in Fig. 2 (c) for the unrelaxed configuration.

The terrace plane plays a key role in determination of the Burgers vector and spatial density of the disconnection defects as well as the twinning dislocations in NiTi. In order to evaluate the step height and Burgers vector content of the interface, the transformation mapping matrices relating the B2 and B19' lattices as shown in the reference configuration of Fig. 2 (c) are constructed. The defect density residing on the terrace plane accommodates the planar misfit strains introduced due to the orientation and lattice constant differentials between two abutting crystals. The planar misfit strains are expressed in Eqs. (1) and (2) in terrace plane coordinate frame of $e_1 - e_2 - e_3$,as shown in Fig. 2 (c),as follows:

$$\varepsilon_{11} = \frac{d_{(010)_M} - 2d_{(1\overline{1}0)}}{\left(d_{(010)_M} + 2d_{(1\overline{1}0)}\right)\Big/2} \tag{1}$$

$$\varepsilon_{22} = \frac{d_{(\overline{1}00)_M} - d_{(00\overline{1})}}{\left(d_{(\overline{1}00)_M} + d_{(00\overline{1})}\right)\Big/2} \tag{2}$$

which correspond to $\varepsilon_{11} = 3.43\%$ and $\varepsilon_{22} = 4.97\%$.

Considering the cubic and monoclinic structures of the austenite and martensite phases, the matrix **Q** maps the coordinates in the monoclinic skeletal lattice to the orthonormal austenite coordinate frame of $[110] - [\overline{1}00] - [\overline{1}10]$shown in Fig. 2 (b) as:

$$Q = \frac{1}{a_0} \begin{bmatrix} a & 0 & 0 \\ 0 & b & 0 \\ c\cos\beta & 0 & c\sin\beta \end{bmatrix} \quad (3)$$

The transformation mapping, **M** from the austenite coordinate frame to the martensite frame($[100]_M - [010]_M - [001]_M$) can be as expressed as $M = Q^{-1}A$ where the orthogonal coordinate transformation matrix A is equal to:

$$A = \frac{1}{\sqrt{2}} \begin{bmatrix} 1 & -1 & 0 \\ 0 & 0 & -1 \\ 1 & 1 & 0 \end{bmatrix} \quad (4)$$

As illustrated in Fig. 3, the disconnection type of defects reside on the terrace plane composed of a Burgers vector, b^D, and a surface step height, h. Based on the difference between the translational symmetry vectors of the two phases normal to the terrace plane, the vector b^D can be calculated as:

$$b^D = [110] - [001]_M M^T = \begin{bmatrix} 0.5473 & \overline{0.2536} & \overline{0.2536} \end{bmatrix} \text{ Angstroms} \quad (5)$$

in the austenite frame. The superscript "T" stands for transpose operation. It is to be noted that throughout the present work, the tensorial objects provided without any subscript, with "TP" and "M" subscripts correspond to austenite crystal frame, terrace plane coordinate frame and martensite crystal frames respectively. To this end, the vector b^D is expressed in the terrace plane, TP, coordinate frame as:

$$b^D = \begin{bmatrix} 0 & \overline{0.5473} & \overline{0.3536} \end{bmatrix}_{TP} \text{ Angstroms} \quad (6)$$

On the other hand, the step height, h, corresponds to $2d_{(110)} = 4.2638$ Angstroms. Considering that the component of b^D along e_1 is zero, the disconnection spacing which accommodates for the misfit strain ε_{22} is evaluated to be equal to:

$$d^D = \frac{|b^D \cdot e_2|}{\varepsilon_{22}} = 11.01 \text{ Angstroms} \quad (7)$$

In order to determine the habit plane by the TM in a self-consistent manner, the lattice invariant shear and the

corresponding lattice rotation should be incorporated into the theoretical calculations complying with the experimental measurements. The High Resolution TEM (HRTEM) imaging studies show that in majority the Type II-1 twins dominate in martensite phase of NiTi shape memory alloy [51]. Following up on this experimental evidence, we modeled the lattice invariant shear accommodating ε_{11} strain component via introducing $b^{LIS} = 1/9[011]_M$ Burgers vectors on consecutive $(0.72054\,1\,\overline{1})_M$ planes [50,52,53]. Based on this geometric condition, the spacing of b^{LIS}, i.e. denoted as d^{LIS}, is calculated to be equal to:

$$d^{LIS} = \frac{|b^{LIS} \cdot e_1|}{\varepsilon_{11}} = 11.57 \text{ Angstroms} \quad (8)$$

As there are two types of defects, i.e. disconnections on the terrace plane and the Type II-1 twinning dislocations residing on $(0.72054\,1\,\overline{1})_M$ twin planes, the net rotation tensor, R, can be expressed as the combined action of the individual rotation tensors associated with the displacement fields of these defects, i.e. R_1 and R_2, as:

$$R = R_2 R_1 \quad (9)$$

On geometrical grounds, the rotation axes of these tensors coincide with the unit ω_1 and ω_2 vectors which correspond to:

$$\omega_1 = \xi^D \quad (10)$$

$$\omega_2 = \xi^{LIS} x N \quad (11)$$

where

$$\xi^D = \begin{bmatrix} 0.7071 & \overline{0.7071} & 0 \end{bmatrix} \quad (12)$$

$$\xi^{LIS} = \begin{bmatrix} 0 & 0 & 1 \end{bmatrix} \quad (13)$$

$$N = \begin{bmatrix} 0.4556 & 0.6322 & \overline{0.6268} \end{bmatrix} \quad (14)$$

The rotation angles of ψ_1 and ψ_2 about ω_1 and ω_2 axes are evaluated as:

Fig. 3. (a) Shows the 3-D terrace plane geometry the tangent plane of which corresponds to the macroscopic habit plane considering the net rotation expressed as $R_2 R_1$ in explicit form in Eq. (17) and (18). **(b)** illustrates a closer view on the terrace plane depicting the disconnections composed of step height h and the Burgers vector b^D as well as the twinning dislocations b^{LIS} which accommodate the misfit strains resulting from the differences in the lattice structure and orientation of the austenite and martensite phases.

$$\psi_1 = \tan^{-1}\left(\frac{h}{d^D}\right) \tag{15}$$

$$\psi_2 = \sin^{-1}\left(\frac{\left|b^D \cdot e_3\right|}{2d^D}\right) + \sin^{-1}\left(\frac{\left|b^{LIS} \cdot e_3\right|}{2d^{LIS}}\right) \tag{16}$$

In explicit form, the rotation tensors of R_1 and R_2 are equal to:

$$R_1 = I\cos\psi_1 + \,\in\omega_1 \sin\psi_1 + \omega_1 \otimes \omega_1(1 - \cos\psi_1) \tag{17}$$

$$R_2 = I\cos\psi_2 + \,\in\omega_2 \sin\psi_2 + \omega_2 \otimes \omega_2(1 - \cos\psi_2) \tag{18}$$

where $\in$ is the third order permutation tensor and $\otimes$ is outer product operator. The net rotation acting on the reference terrace plane normal p, i.e. parallel to e_1, leads to the modified terrace plane normal p'. Iterating the procedure constructed by the set of Eqs. (1)–(18) results in the tabulated values of Table 2. It is to be noted that the modified p' vector in this particular case converges to the habit plane normal **n** after the iteration step 2.

The predicted habit plane normal $\mathbf{n} = [0.4531\ 0.2759\ 0.8477]$ deviates from the experimentally measured habit plane normal of $[0.4138\ 0.26878\ 0.8684]$ only by an angle of $3.80°$ and from $[0.4044\ 0.2152\ 0.8888]$ predicted by the PTMC by an angle of $5.12°$ [53]. For a discussion on the habit plane calculations utilizing TM and PTMC, the reader is referred to Refs. [54,55]. In our case, considering the close agreement between the TM theory and the experimental measurements, we delineated the geometry employed in the MS calculations based on the habit plane indices tabulated in Table 2. At this stage, it is to be emphasized that in TM the Burgers vectors associated with the interface dislocations and disconnections are unique within the intersection of the symmetry groups of the abutting crystals. The calculation procedure followed throughout the forward transformation CRSS calculations incorporating the non-Schmid character core glide resistance effects are detailed in the following section.

2.3. Molecular statics calculations

In order to model the glide motion of Burgers vectors residing on the terrace plane, in the present work, we employed MS calculations employing the NiTi interatomic potential. A simulation box size of $120 \times 120\ \text{x}\ 9\,\text{Å}^3$ is oriented along $[100] - [010] - [001]$ triad with periodic boundary conditions imposed on atoms located at the two bounding (001) planes and fixed displacement conditions on the other enclosing boundaries. The reference terrace plane of (110) separates the Type II-1 twinned martensite and the austenite phases as illustrated in Fig. 4. In delineation of the simulation box, a twinning shear magnitude of 0.2804 along the twinning direction of $[011]_M$ is implemented on $(0.72054\ 1\ \overline{1})_M$ twin plane in the martensitic phase. For equiatomic NiTi, the fractions of twins have been demonstrated to be as 0.27 and 0.73 employing the geometrically non-linear theory of martensite transformation [6]. Based on these resulting twin fractions, the

Table 2
Tabulates the habit plane normal p' and the angles ψ_1 and ψ_2 that have been determined in each iteration step. It is to be noted that iteration step 0 corresponds to the reference configuration.

Iteration Step	0 (Initial OR)	1	2
p'	[1 1 0]	[0.5343 0.3640 0.7066]	[0.4531 0.2759 0.8477]
ψ_1	9.06°	14.71°	–
ψ_2	21.41°	28.66°	–

twinning dislocations with a Burgers vector of $b^{LIS} = 1/9[011]_M$ are introduced at an alternating spacing of 3.1 and 8.4 Å apart from the disconnections on the terrace plane. The displacement fields associated with the disconnections and the twinning dislocations are generated inside the simulation box employing the linear elastic anisotropic theory. Subsequently, a relaxation calculation is conducted to incorporate the departures from the elastic theory which are of substantial importance in core disregistry fields. In this formulation, each single dislocation residing at the terrace plane separating the two phases associated with the distinct elastic stiffness tensors of C_{ijkl}^A and C_{ijkl}^M (A:austenite and M: martensite for this particular case) generates a displacement field u_i (i = 1,2,3) of the form in the two domains of austenite (A) and martensite (M):

$$u_i^A(x) = \frac{1}{2\pi\sqrt{-1}} \sum_{\alpha=1}^{6} \eta A_{i\alpha}^A E_\alpha^A \ln(m \bullet x + p_\alpha p \bullet x) \quad p \bullet x > 0 \tag{19}$$

$$u_i^M(x) = \frac{1}{2\pi\sqrt{-1}} \sum_{\alpha=1}^{6} \eta A_{i\alpha}^M E_\alpha^M \ln(m \bullet x + p_\alpha p \bullet x) \quad p \bullet x < 0 \tag{20}$$

where for $\alpha = 1, 2, 3$ the sign of η is chosen as "+" meanwhile it is it is taken as "-" for $\alpha = 4, 5, 6$. The constants of E_α^A and E_α^M are determined by the boundary conditions imposing the continuity of tractions and the displacement jump across the glide plane as will be detailed in the following analysis. In the formulation of Eq. (19) and (20); m corresponds to the unit dislocation line vector (either ξ^D or ξ^{LIS}) and **x** is the position vector corresponding to the point at which the displacement component is calculated. The unit normal **p** of the terrace plane is directed from the martensite towards the austenite phase. It is to be emphasized that Eq. (19) is derived based on the equilibrium condition of Eq. (21) expressed in terms of the displacement field components as:

$$\sigma_{ij,j}^A = C_{ijkl}^A u_{k,lj}^A = 0 \tag{21}$$

To determine the set of complex constants $\{p_\alpha^A, A_{i\alpha}^A\}$ appearing in Eq. (19), the explicit form of Eq. (21) derived within the framework of Eshelby-Stroh formulation is invoked as:

$$C_{ijkm}^A\left(m_i + p_\alpha^A n_i\right)\left(m_m + p_\alpha^A n_m\right)A_{k\alpha}^A = 0 \tag{22}$$

where

$$\det\left\{C_{ijkm}^A\left(m_i + p_\alpha^A n_i\right)\left(m_m + p_\alpha^A n_m\right)\right\} = 0 \tag{23}$$

Similarly, for the martensitic phase, the equilibrium condition imposed on the stress field, as expressed in Eq. (24), leads to Eq. (25) and (26) for a non-trivial solution of $\{p_\alpha^M, A_{i\alpha}^M\}$:

$$\sigma_{ij,j}^M = C_{ijkl}^M u_{k,lj}^M = 0 \tag{24}$$

$$C_{ijkm}^M\left(m_i + p_\alpha^M n_i\right)\left(m_m + p_\alpha^M n_m\right)A_{k\alpha}^M = 0 \tag{25}$$

where

$$\det\left\{C_{ijkm}^M\left(m_i + p_\alpha^M n_i\right)\left(m_m + p_\alpha^M n_m\right)\right\} = 0 \tag{26}$$

At this stage, it is to be emphasized that $\{p_1^A, p_2^A, p_3^A\}$ and $\{p_4^A, p_5^A, p_6^A\}$ are the complex conjugates of each other so as the sets of $\{p_1^M, p_2^M, p_3^M\}$ and $\{p_4^M, p_5^M, p_6^M\}$. Provided the independent elastic stiffness
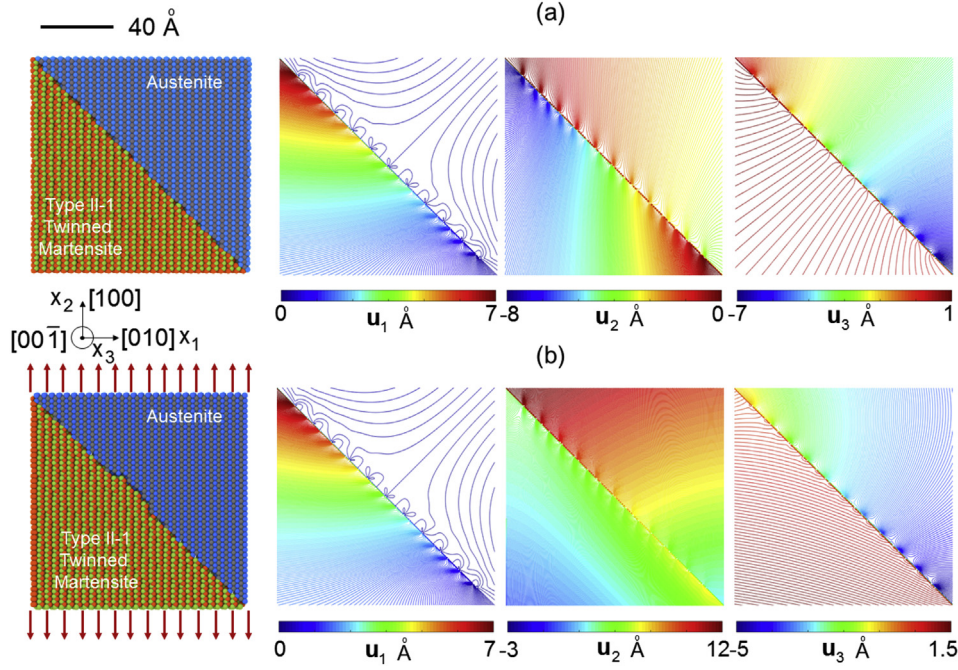
Fig. 4. (a) Shows the externally stress free configuration of the simulation box along with the initial displacement field employed for introducing the Burgers vector content associated with the disconnections and twinning dislocations via anisotropic linear elasticity. **(b)** shows the same simulation box under uniaxial [100] tensile external stress field corresponding to 5% axial strain. This configuration also corresponds to the migration of austenite-martensite interface favoring the martensite volume fraction increase.

tensor components for the NiTi interatomic potential [44]which are tabulated in Table 3, the numerical solutions for the sets of $\{p_1^A, p_2^A, p_3^A\}$ and $\{p_1^M, p_2^M, p_3^M\}$are shown in Table 4.

In order to determine the anisotropic parameters ofE_α^A and E_α^M, the two sets of boundary conditions are employed. The expressions in Eq. (27) and (28) impose the continuity of the normal tractions across the interface and the displacement field respectively as follows:

$$\sum_{\alpha=1}^{6} A_{i\alpha}^A E_\alpha^A - \sum_{\alpha=1}^{6} A_{i\alpha}^M E_\alpha^M = 0 \quad (i = 1, 2, 3) \tag{27}$$

$$\sum_{\alpha=1}^{6} L_{i\alpha}^A E_\alpha^A - \sum_{\alpha=1}^{6} L_{i\alpha}^M E_\alpha^M = 0 \quad (i = 1, 2, 3) \tag{28}$$

where $L_{i\alpha}^A$ and $L_{i\alpha}^M$ are expressed as:

$$L_{i\alpha}^A = -p_j C_{ijkm}^A \left(m_m + p_\alpha^A n_m \right) A_{k\alpha}^A \tag{29}$$

$$L_{i\alpha}^M = -p_j C_{jikm}^M \left(m_m + p_\alpha^M n_m \right) A_{k\alpha}^M \tag{30}$$

On the other hand, the absence of a line force inside the core region and the presence of a displacement jump quantified by the components of a generic Burgers vector b (it can either be of b^D or b^{LIS} depending on the particular displacement field evaluated) dictate Eq. (31) and (32) respectively.

$$\sum_{\alpha=1}^{6} \eta L_{i\alpha}^A E_\alpha^A + \sum_{\alpha=1}^{6} \eta L_{i\alpha}^M E_\alpha^M = 0 \quad (i = 1, 2, 3) \tag{31}$$

$$\sum_{\alpha=1}^{6} \eta A_{i\alpha}^A E_\alpha^A + \sum_{\alpha=1}^{6} \eta A_{i\alpha}^M E_\alpha^M = 2b_i \quad (i = 1, 2, 3) \tag{32}$$

It is to be noted that the multiplier η is taken as "+1" and "-1" for $\alpha = \{1, 2, 3\}$ and $\alpha = \{4, 5, 6\}$ respectively. The twelve unknowns of $E_{i\alpha}^A$ and $E_{i\alpha}^M$ are solved based on the twelve equations introduced in Eqs. (25), (26), (29) and (30). The resulting values are tabulated in Table 5.

The configuration within the absence of externally applied stresses is shown in Fig. 4 (a) which is generated upon relaxation of the plotted displacement component fields described by Eq. (19) and (20). Moreover, we implemented the homogeneous uniaxial stress field upon the configuration of Fig. 4 (a)via superimposing the corresponding displacement components described within the framework of the anisotropic linear elastic theory in Eq. (33):

$$\frac{\partial u_i}{\partial x_j} + \frac{\partial u_j}{\partial x_i} = 2S_{ijkl}\sigma_{kl}^\infty \tag{33}$$

where $S_{ijkl}$is the fourth order elastic compliance tensor. Eq. (33) allows us to bridge the homogeneous applied stress field, σ_{kl}^∞, and the related displacement gradients subjected to appropriate coordinate transformation operations. The σ_{kl}^∞ components are

Table 3
The independent elastic stiffness tensor components of austenite and martensite phases, i.e. C_{ij}^A and C_{ij}^M (i,j = 1 to 6) in Voigt notation determined by the NiTi potential, are tabulated in units of GPa [44].

C_{11}^A	C_{12}^A	C_{44}^A	C_{11}^M	C_{12}^M	C_{13}^M	C_{15}^M	C_{22}^M	C_{23}^M	C_{25}^M	C_{33}^M	C_{35}^M	C_{44}^M	C_{64}^M	C_{55}^M	C_{66}^M
146	122	35	218	120	103	−16	252	72	−7	206	2	37	−2	41	43

Table 4
Tabulates the complex parameters of p_α^A and p_α^M for the austenite and martensite phases where $i = \sqrt{-1}$.

p_1^A	p_2^A	p_3^A	p_1^M	p_2^M	p_3^M
$0 + i$	$0.77 + 0.63i$	$-0.77 + 0.63i$	$-0.62 + 0.78i$	$0.03 + 0.99i$	$0.67 + 0.74i$

Table 5
Tabulates the complex parameters of E_α^A and E_α^M where $\alpha = 1$ varies to 6 and $i = \sqrt{-1}$.

E_1^A	E_2^A	E_3^A	E_4^A	E_5^A	E_6^A
$-0.06 + 0i$	$0.49 + 0.13i$	$0.11 + 0.55i$	$0.06 + 0i$	$-0.49 + 0.13i$	$-0.11 + 0.55i$

E_1^M	E_2^M	E_3^M	E_4^M	E_5^M	E_6^M
$13.46 + 23.34i$	$4.49 + 6.71i$	$8.82 + 19.28i$	$-13.46 + 23.34i$	$-4.49 + 6.71i$	$-8.82 + 19.28i$

proportionally increased till the glide of the transformation front initiates. In Fig. 4 (b), the deformed configuration of the simulation box under uniaxial tension along [100], at a level of 5% axial strain, is shown along with the corresponding displacement component fields. Similarly, in the present work, [110], [111], [122] and [012] uniaxial tension cases are also simulated employing MS calculations. The experimentally measured CRSS levels and the habit planes for these single crystals are tabulated in Table 6 [7]. The MS calculations conducted in this approach provides atomistic scale short-range energy and core disregistry information. This enables us to calculate the theoretical CRSS levels for forward transformation employing the modified Peierls-Nabarro framework as will be further expounded in the subsequent sections.

2.4. Modified Peierls-Nabarro framework and quantification of CRSS levels

In order to pinpoint the CRSS levels for the motion of the transformation front under external stress tensor field corresponding to uniaxial tensile loading along the [100], [110], [111], [122] and [012] directions, we conducted modified Peierls-Nabarro calculations considering the periodic defect content of the transformation front. In order to accomplish this task, as a function of sample orientation, a total energy functional E^{tot}, the maximum gradient of which with respect to the core disregistry fields corresponds to theoretical CRSS levels is derived. In this framework, the resolved shear stress acting along the shape strain direction at the critical loading step initiating the transformation front glide is designated as the forward CRSS for transformation.

E^{tot} functional is composed of both long range energy terms: elastic strain energy associated with the defect array at the transformation front, i.e. E^e, and the applied work, W, as well as the short range energy terms such as the transformation energy profile from B2 to B19' structure, i.e. E^{trans}, the planar fault energy associated with the glide of Type II-1 twinning dislocations, i.e. E^{twin}, and the misfit energy introduced by the glide motion of the

disconnections, i.e. E^{mis}. Therefore, E^{tot} expression can be explicitly written as:

$$E^{tot} = E^e + E^{trans} + E^{twin} + E^{mis} - W \tag{34}$$

Among the short range energy terms, the transformation energy versus the transformation displacement on the basal plane {110} <001>, denoted as u, is adapted from the earlier ab-initio calculations of Wang et al. [56] in Fig. 5 (a). On the other hand, the glide motion of the $1/9[110]_M$ twinning dislocations on the consecutive planes of $(0.72054\,1\,\overline{1})_M$ is governed by the generalized planar fault energy (GPFE) profile for Type II-1 twins of martensite phase. The corresponding energy profile, i.e. denoted as γ_3 curve in present work, is plotted in Fig. 5(b) based on the ab-initio calculations of Ezaz et al. [52]. The GPFE profile in Fig. 5 (b) can be expressed as a function of the core disregistry field associated with the twinning dislocation as follows in Eq. (35) where m is an integer and d_3 is the translational periodicity vector along $[011]_M$ indicating $\gamma_3 : \gamma_3(t + md_3)$.

$$E^{twin} = \sum_{m=-\infty}^{\infty} \gamma_3(t + md_3)d_3 \tag{35}$$

The shear induced glide motion for disconnection Burgers vector b^D can be initiated by its dissociation along <100>{110} and <111> {110} glide systems which exhibit much lower energy barriers on the generalized stacking fault energy (GSFE) surface compared to the other potential systems (within the absence of thermally activated mechanisms). Therefore, the dissociation reaction for b^D is expressed as:

$$\underbrace{\left[0.5473\,\overline{0.2536}\,\overline{0.2536}\right]}_{b^D} \rightarrow \underbrace{0.2937[101]}_{b_1} + \underbrace{0.2536[1\overline{1}\,\overline{1}]}_{b_2} \tag{36}$$

Based on this dissociation reaction in Eq. (36), the misfit energy can be expressed as:

Table 6
The experimental CRSS levels of transformation under uniaxial loading for 51.5% at. Ni− NiTi shape memory alloy is tabulated [7].

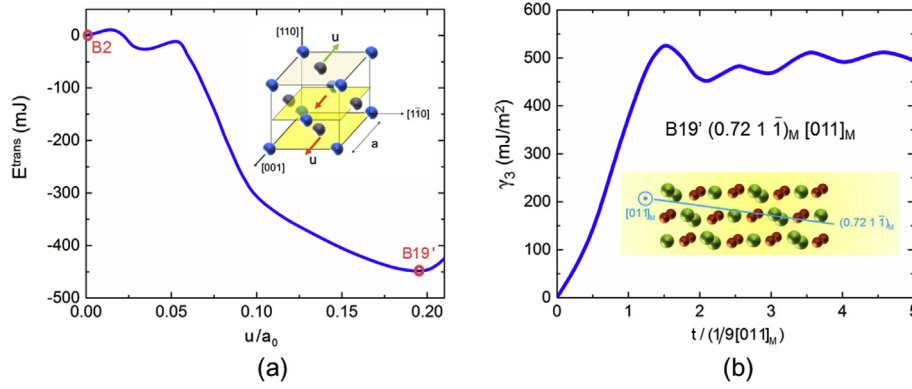| Loading Orientation	[100]	[110]	[111]	[122]	[012]
CRSS (Transformation)	270 MPa	370 MPa	240 MPa	285 MPa	360 MPa
Measured Habit Plane	$\begin{pmatrix} 0.8889 \\ 0.4044 \\ 0.2152 \end{pmatrix}$	$\begin{pmatrix} 0.8889 \\ 0.2152 \\ \overline{0.4044} \end{pmatrix}$	$\begin{pmatrix} \overline{0.2152} \\ 0.4044 \\ 0.8889 \end{pmatrix}$	$\begin{pmatrix} \overline{0.2152} \\ 0.8889 \\ 0.4044 \end{pmatrix}$	$\begin{pmatrix} \overline{0.4044} \\ 0.2152 \\ 0.8889 \end{pmatrix}$

Fig. 5. (a) The *ab-initio* generated transformation energy profile shown as a function of the total transformation displacement along the multilayers of {110} <001> system based on the earlier work of Wang et al. [56]. (b)The generalized planar fault energy (GPFE) curve generated via the glide of $1/9[011]_M$ twinning dislocations on the consecutive $(0.72054\ 1\ \bar{1})_M$ planes based on the earlier work of Ezaz et al. [52].

$$E^{mis} = E_1 + E_2 = \sum_{m=-\infty}^{\infty} \gamma_1(s + md_1)d_1 + \sum_{m=-\infty}^{\infty} \gamma_2(v + md_2)d_2 \tag{37}$$

where E_1 and E_2 are the generalized stacking fault energies introduced by the Burgers vectors of b_1 and b_2 during the shear glide of transformation front as plotted in Fig. 6(a) and (b). In Eq. (37), d_1 and d_2 are the translational periodicity vector magnitudes along <100> and <111> directions representing the periodic characters of $\gamma_1 : \gamma_1(s + md_1)$ and $\gamma_2 : \gamma_2(v + md_2)$. In explicit terms, these energy expressions can be described as a function of the disregistry functions which are mathematical manifestations of the spatially smeared out Burgers vectors within the close proximity of the defect cores in relation with the corresponding GSFE profiles.

To determine the theoretical transformation CRSS levels as a function of uniaxial loading direction, the Burgers vectors of both b_1, b_2 and b^{LIS} are described as continuous spatial disregistry functions based on the relaxed core displacement fields generated employing the MS calculations. The disregistry fields associated with b_1, b_2 and b^{LIS} can be explicitly expressed as:

$$f_1(s) = \frac{b_1}{\pi}\left[\tan^{-1}\left(\frac{s - s_1}{c_1\zeta_1}\right) + (c_1 - 1)\zeta_1\frac{s - s_1}{(s - s_1)^2 + (c_1\zeta_1)^2}\right] + \frac{b_1}{2} \tag{38a}$$

$$f_2(v) = \frac{b_2}{\pi}\left[\tan^{-1}\left(\frac{v - v_2}{c_2\zeta_2}\right) + (c_2 - 1)\zeta_2\frac{v - v_2}{(v - v_2)^2 + (c_2\zeta_2)^2}\right] + \frac{b_2}{2} \tag{38b}$$

$$f_3(t) = \frac{b^{LIS}}{\pi}\left[\tan^{-1}\left(\frac{t - t_3}{c_3\zeta_3}\right) + (c_3 - 1)\zeta_3\frac{t - t_3}{(t - t_3)^2 + (c_3\zeta_3)^2}\right] + \frac{b^{LIS}}{2} \tag{38c}$$

where $\{s, v, t\}$ are the parametric coordinates along the glide direction of each individual defect and $\{s_1, v_2, t_3\}$ are the line center positions. The set of free parameters $\{c_1, \zeta_1, c_2, \zeta_2, c_3, \zeta_3\}$ convey information regarding the defect core widths as a function of loading direction. These free parameters are determined by the regression of the relaxed displacement field on the habit plane extracted from the MS simulations. It is to be noted that the following conditions are satisfied for each disregistry function:

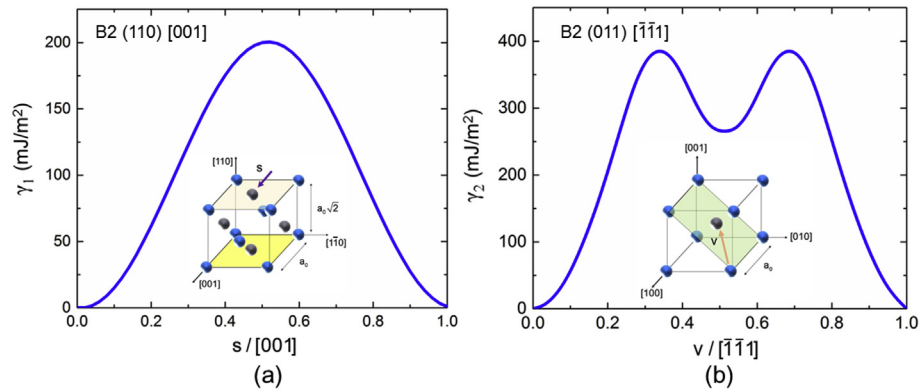$$\int_{-\infty}^{\infty}\frac{\partial f_1}{\partial s}\,ds = b_1 \tag{39a}$$

Fig. 6. (a) Shows the GSFE profile along (110) [001] in equiatomic NiTi [48]via the NiTi potential employed in the present study. (b) shows the GSFE profile generated along the $(011)[\bar{1}\bar{1}1]$ glide system via the NiTi potential employed in the current work. At this stage, it is to be emphasized that the system $(011)[\bar{1}\bar{1}1]$ is prone to generate intrinsic stacking faults unlike the (110) [001] system. The lower unstable stacking fault energy along (110) [001] favors it as the prevalent glide system of near equiatomic NiTi as demonstrated experimentally in Ref. [48].

$$\int_{-\infty}^{\infty} \frac{\partial f_2}{\partial v} dv = b_2 \tag{39b}$$

$$\int_{-\infty}^{\infty} \frac{\partial f_3}{\partial t} dt = b^{LIS} \tag{39c}$$

The long range energy term is composed of the elastic strain energy, E^e, of the interfacial defect array. The resultant elastic line energy expression is given as (k, j = 1,2,3) [45]:

$$E^e = \int_{-\infty}^{\infty} \frac{\partial f_1}{\partial s} S_k \sigma_{kj} p_j ds + \int_{-\infty}^{\infty} \frac{\partial f_2}{\partial v} V_k \sigma_{kj} p_j dv + \int_{-\infty}^{\infty} \frac{\partial f_2}{\partial t} T_k \sigma_{kj} p_j dt \tag{40}$$

where the vectors of S, V and T are the unit tangent vectors parallel to the Burgers vectors of b_1, b_2 and b^{LIS} respectively. The resultant stress tensor components, σ_{jk}, appearing in Eq. (40) can be expressed as:

$$\sigma_{jk} = \sigma_{jk}^{\infty} + \sigma_{jk}^1 + \sigma_{jk}^2 + \sigma_{jk}^{LIS} \tag{41}$$

where the stress tensor components associated with the Burgers vectors of b_1, b_2 and b^{LIS} are explicitly given as:

$$\sigma_{jk}^1 = \frac{d^D}{2} \Big\{ \sum_{i=1}^{3} \Big(L_{kj}^M E_i^A + L_{kj}^A E_i^M\Big)\kappa_1 - \sum_{i=1}^{3} \Big(L_{kj}^A E_i^M + L_{kj}^M E_i^A\Big)\phi_1$$
$$- \sum_{i=1}^{3} sign\Big[x_2\Big(L_{jk}^M E_i^A - L_{jk}^A E_i^M\Big)\Big]\Big\} \tag{42a}$$

$$\sigma_{jk}^2 = \frac{d^D}{2} \Big\{ \sum_{i=1}^{3} \Big(L_{kj}^M E_i^A + L_{kj}^A E_i^M\Big)\kappa_2 - \sum_{i=1}^{3} \Big(L_{kj}^A E_i^M + L_{kj}^M E_i^A\Big)\phi_2$$
$$- \sum_{i=1}^{3} sign\Big[x_2\Big(L_{jk}^M E_i^A - L_{jk}^A E_i^M\Big)\Big]\Big\} \tag{42b}$$

$$\sigma_{jk}^{LIS} = \frac{d^{LIS}}{2} \Big\{ \sum_{i=1}^{3} \Big(L_{kj}^M E_i^A + L_{kj}^A E_i^M\Big)\kappa_{LIS} - \sum_{i=1}^{3} \Big(L_{kj}^A E_i^M + L_{kj}^M E_i^A\Big)\phi_{LIS}$$
$$- \sum_{i=1}^{3} sign\Big[x_2\Big(L_{jk}^M E_i^A - L_{jk}^A E_i^M\Big)\Big]\Big\} \tag{42c}$$

where "sign [ ]" stands for the signum function. The sets of variables $\{\phi_1, \phi_2, \phi_{LIS}\}$ appearing in Eq. (42) are given as:

$$\phi_1 = \Big[\sinh(2\pi)d^D p_i^A\Big(x_1 + p_i^A x_2\Big)\Big] \Big/ \Big[\cosh(2\pi)d^D p_i^A x_2$$
$$- \cos(2\pi)d^D\Big(x_1 + p_i^M x_2\Big)\Big] \tag{43a}$$

$$\phi_2 = \Big[\sinh(2\pi)d^D p_i^A\Big(x_1 + p_i^A x_2\Big)\Big] \Big/ \Big[\cosh(2\pi)d^D p_i^A x_2$$
$$- \cos(2\pi)d^D\Big(x_1 + p_i^M x_2\Big)\Big] \tag{43b}$$

$$\phi_{LIS} = \Big[\sinh(2\pi)d^{LIS} p_i^A\Big(x_1 + p_i^A x_2\Big)\Big] \Big/ \Big[\cosh(2\pi)d^{LIS} p_i^A x_2$$
$$- \cos(2\pi)d^{LIS}\Big(x_1 + p_i^M x_2\Big)\Big] \tag{43c}$$

meanwhile the set of variables $\{\kappa_1, \kappa_2, \kappa_{LIS}\}$ corresponds to:

$$\kappa_1 = \Big[\sinh(2\pi)d^D p_i^A x_2\Big] \Big/ \Big[\cosh(2\pi)d^D p_i^A x_2 - \cos(2\pi)d^D\Big(x_1$$
$$+ p_i^M x_2\Big)\Big] \tag{44a}$$

$$\kappa_2 = \Big[\sinh(2\pi)d^D p_i^A x_2\Big] \Big/ \Big[\cosh(2\pi)d^D p_i^A x_2 - \cos(2\pi)d^D\Big(x_1$$
$$+ p_i^M x_2\Big)\Big] \tag{44b}$$

$$\kappa_{LIS} = \Big[\sinh(2\pi)d^{LIS} p_i^A x_2\Big] \Big/ \Big[\cosh(2\pi)d^{LIS} p_i^A x_2$$
$$- \cos(2\pi)d^{LIS}\Big(x_1 + p_i^M x_2\Big)\Big] \tag{44c}$$

Lastly, the term, W, is defined as the work done on the three glide systems of b_1, b_2 and b^{LIS} Burgers vectors by the resolved applied glide shear stresses. On mathematical grounds, this is expressed as:

$$W = (b_1)_k \sigma_{kj}^{\infty} p_j + (b_2)_k \sigma_{kj}^{\infty} p_j + \Big(b^{LIS}\Big)_k \sigma_{kj}^{\infty} N_j \tag{45}$$

Following the construction of the E^{tot} functional, the forward CRSS is determinated as the maximum of the normalized glide resistance among the three concerted disregistry distributions $f_1(s)$, $f_2(v)$ and $f_3(t)$ which are formulated as:

$$CRSS = \max\left(\frac{1}{\max(f_i)} \frac{\partial E^{tot}}{\partial f_i}\right)\Lambda \quad (i = 1, 2, 3) \tag{46}$$

where the trigonometric factor Λ projects the maximum normalized gradient of the total energy functional to the active habit plane - shape strain system following the convention for the reported CRSS levels in the earlier literature [7].

3. Modeling results

In this section, the MS simulation results are provided which give a detailed theoretical insight on the interaction between the uniaxial loading direction and the interface defect core structures. The relaxed differential displacements among the neighboring atoms at the interface calculated via MS simulations for the externally stress-free and uniaxially loaded configurations are of paramount importance in generating the parametric disregistry fields of $f_1(s)$, $f_2(v)$ and $f_3(t)$. Based on this rationale, in Fig. 7, we plot the differential displacement maps (DDM) formed within the close neighborhood of the habit plane of equiatomic NiTi in externally stress-free and uniaxial [100] tension case as a demonstration of the methodology implemented. In the DDM technique, the normalized relative interatomic displacements which exhibit the same trend as the displacement gradients, are projected along a specific direction; therefore allowing us to represent the corresponding 3-D field on a particular plane [57]. In this study, the relative displacements between the neighboring atoms are projected on the normalized b_1 direction and the length of the pointing arrow is proportional to its magnitude. It is to be noted that similar analogy can be also established for either b_2 or b^{LIS} vectors.
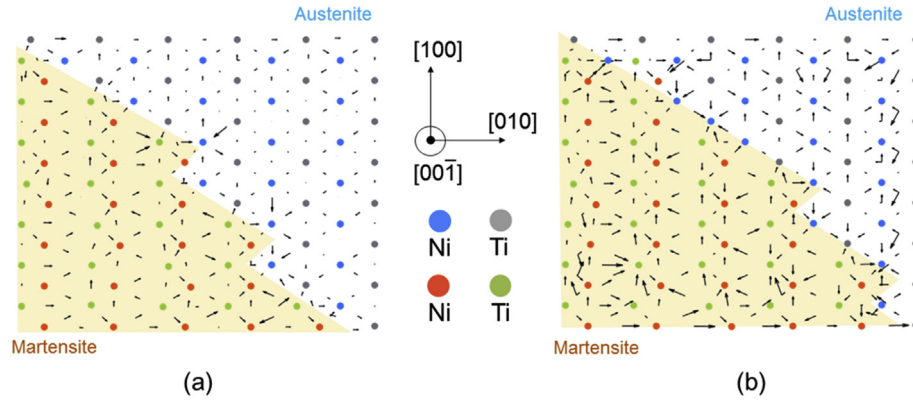
Fig. 7. **(a)** Shows the relaxed differential displacement field projected on $(00\bar{1})$ plane in externally stress-free configuration. **(b)** shows the relaxed differential displacement field projected on $(00\bar{1})$ plane under uniaxial tension along [100] corresponding to an axial strain magnitude of 5%. It is to be noted that as a result of applied loading, the volume fraction of martensite increases which is a consequence of shear-coupled motion of the disconnections and the migration of Type II-1 twins accompanying.

As can be seen in Fig. 7 (a), in the externally-stress free configuration, the relaxed displacements are mainly concentrated in the martensitic structure. The presence of Type II-1 twins has a significant role in this behavior. Furthermore, the localized displacements on the disconnection steps are associated with the disconnection Burgers vectors. As shown in Fig. 7 (b), the DDM plot exhibits intense localizations within the close proximity of the austenite-martensite interface under a uniaxial external stress field along [100] (at a 5% axial strain magnitude). The elastic misfit strains associated with the differential in the elastic constants of the two phases as well as the glide of disconnections and twinning dislocations accompanying the martensitic transformation are responsible from these localizations.

The set of free parameters $\{c_1, \zeta_1, c_2, \zeta_2, c_3, \zeta_3\}$ corresponding to [100], [110], [111], [122] and [012] uniaxial tension cases are determined by multi-linear regression of the relaxed displacement fields at the habit plane. The resulting values are tabulated in Table 7 along with the central points of s_1, v_2 and t_3. Moreover, the corresponding theoretical CRSS levels are included in Table 7. The free parameters exhibit anisotropic behavior reflected by the varying core shapes as a function of loading direction. In order to visualize this difference in core spreading, the concept of infinitesimal dislocation density which is initially introduced by Eshelby [58] is visited. On mathematical grounds, the infinitesimal dislocation density, ρ_i, for a disregistry field of f_i (i = 1,2,3) is defined as:

$$\rho_1 = \frac{\partial f_1(s)}{\partial s} \tag{47a}$$

$$\rho_2 = \frac{\partial f_2(v)}{\partial v} \tag{47b}$$

$$\rho_3 = \frac{\partial f_3(t)}{\partial t} \tag{47c}$$

Following the regressed free parameters and the experimentally measured CRSS levels, the core spreadings at the habit plane are shown for the two tension sample orientations of [100] and [110]. These two cases are particularly chosen as the experimental forward transformation CRSS levels exhibit almost a 100 MPa differential in between. The infinitesimal dislocation densities are plotted as a function of spatial coordinates for the [100] sample in Fig. 8 (a) as well as for the [110] sample in Fig. 8(b) employing differential displacements from MS simulations. Close examination of both plots show that the max. intensities of the dislocation densities and the core widths differ significantly in these two benchmark cases. For example, meanwhile the max (ρ_2) is $0.21b_2$ for the [001] sample, it drops drastically to $0.10\ b_2$ for the [110] sample implying a smeared out disregistry field for the [001] sample.

4. Discussion

The present work presents a novel approach to the determination of CRSS for forward transformation in shape memory alloys focusing on the particular case of the well−known NiTi. In the present work, the key role of the defect content at the habit plane structure is determined by employing the topological model and the anisotropic elasticity in addition to the MS relaxation calculations. The resulting CRSS levels for the forward martensitic transformation are plotted as a function of single crystal loading orientation in Fig. 9 along with the experimentally measured values which are also tabulated in Table 5. The close agreement with the experimental measurements indicate the robustness of the methodology adopted. Both experimental measurements and theoretical calculations demonstrate that forward transformation CRSS levels exhibit an increase towards the [110] pole. On the other hand, the CRSS levels drop by approaching the [100]-[111] symmetry line. This trend can be ascribed to the distinct spreading of the defect cores under varying applied loading directions as demonstrated in Fig. 8. Increasing of the core width and smeared out disregistry intensities are prone to lower the forward transformation CRSS magnitudes. At this stage it is to be noted that the large deformation gradients localized at the defect cores necessitate the short-

Table 7
The set of free parameters in Eq. (38) fitted from the differential displacement mappings of the molecular statics calculations as a function of crystallographic uniaxial loading direction. The theoretical CRSS levels are also included. The 'T' symbol stands for tension.

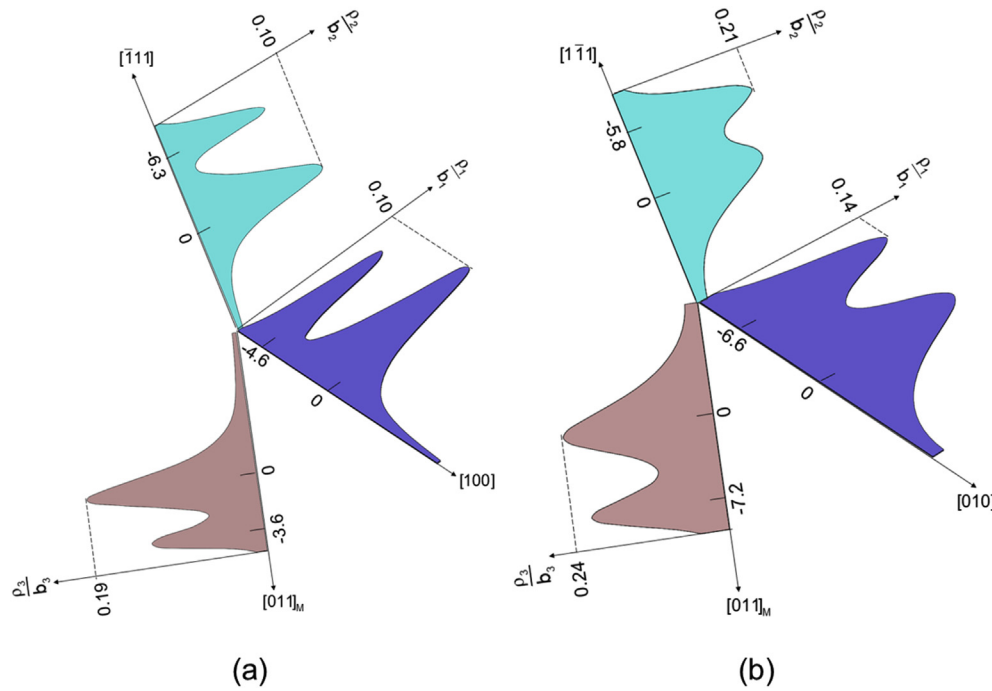|	[100] T	[110] T	[111] T	[122] T	[012] T
c_1	4.3	3.1	4.5	4.0	3.7
ζ_1	2.3	1.5	2.6	2.0	1.7
c_2	3.8	2.9	4.1	3.2	2.9
ζ_2	2.9	2.0	3.3	2.7	2.3
c_3	2.9	1.9	3.2	2.6	2.2
ζ_3	3.3	2.1	3.6	4.9	2.6
s_1/a_0	−6.6	−4.6	−5.3	0.6	−3.6
v_2/a_0	−5.8	−6.3	−4.5	2.7	−1.6
t_3/a_0	−7.2	−3.6	−3.0	−5.6	−3.3
CRSS (Theory)	290 MPa	380 MPa	225 MPa	300 MPa	340 MPa

Fig. 8. (a) Shows the three dislocation density fields of ρ_1, ρ_2 and ρ_3 corresponding to the [100] tension sample. The maximum among the densities is evaluated at ρ_3 (twinning dislocation density) with an intensity of 0.19. Meanwhile, ρ_1 and ρ_2 intensities exhibit a 0.10 peak level. **(b)** shows the three dislocation density fields of ρ_1, ρ_2 and ρ_3 corresponding to the [110] tension sample. Distinguishingly from the [100] tension sample, the maximum ρ_3 intensity level corresponds to 0.24 meanwhile the peak levels of ρ_1 and ρ_2 are 0.14 and 0.21 for the [110] sample. The high intensities of the disregistry fields in the [110] sample is reflected as a significant elevation in CRSS levels as can be seen in Table 5 and Fig. 9.
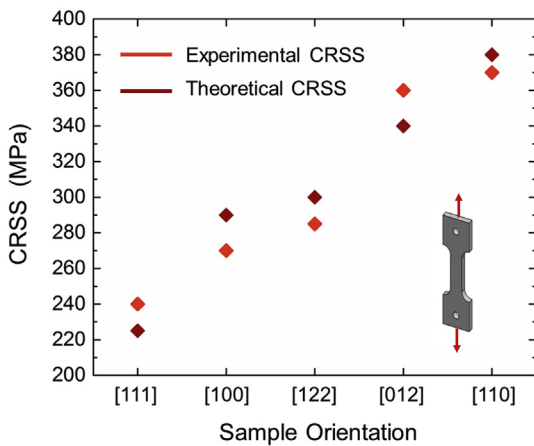
Fig. 9. The experimental measurements of forward transformation CRSS levels for 51.5 at.% Ni-NiTi [7] and the theoretical predictions evaluated based on the modified Peierls-Nabarro framework is plotted as a function of single crystal orientation subjected to uniaxial tension. The corresponding habit planes are also tabulated in Table 5.

range interatomic interactions to be accurately described in addition to the long range energy terms. To this end, the atomistically informed disregistry fields substituted into the GPFE and GSFE energy profiles play a key role in the accuracy of the resulting transformation CRSS levels.

Fig. 9 shows that the non-Schmid transformation response in NiTi can lead to more than 160 MPa stress differential among the sample orientations simulated based on the available experimental data which corresponds to a 72% relative anisotropic difference. The extent of this deviation from Schmid law is very substantial and should be considered in any modeling efforts with NiTi shape memory alloy. Many of the polycrystalline NiTi materials undergo

drawing or rolling operations and possess a [111] crystallographic texture [59], i.e. the majority of the grains are oriented in the [111] direction. An intrinsically low CRSS for transformation with moderate plastic slip resistance [5,60] translates to a favorable functionality for the [111] case compared to other orientations.

The description of the transformation stress does not conform to a single constant CRSS criterion for NiTi as the dislocation and disconnection network reticulating the habit plane exhibit nonplanar core spreading. As an outcome, any of the resolved stresses acting along the three disregistry fields of $f_1(s)$, $f_2(v)$ and $f_3(t)$ may dictate the CRSS level considering the intricate nature of the displacement pattern developed. Close examination of the presented results reveal that smeared out disregistry fields facilitate the transformation front motion which is reflected by a lower CRSS level. A similar effect has also been identified in the glide behavior of screw dislocations in an earlier work focusing on slip mediated plasticity in NiTi [48]. Among the previous treatments focusing on martensitic transformation pathways, the role of dislocations is emphasized profoundly in the Bogers-Burgers mechanism [61]. On the other hand, the earlier literature invoking this mechanism has evolved around the fcc to hcp and bcc to hcp transformations [62,63]. As a novelty, in the present work, we employed the TM in characterizing the role of interfacial defects in martensitic transformation of NiTi from B2 to B19' with a Type II-1 twinned microstructure. The faceted structure of the habit plane imposes consideration of the disconnections in addition to the dislocations. Furthermore, as the climb component of disconnection Burgers vector is necessary in advancing the transformation front [54], the complete external stress tensor in addition to the glide shear stress term is necessary in the theoretical calculations. In the present work, this task is accomplished by providing the atomistically informed defect core disregistry fields into the total energy functional which enables us to calculate the theoretical forward transformation CRSS levels without any empirical

constants. Moreover, consideration of the complete applied stress tensor enables us to predict the anisotropy involved in the theoretical CRSS magnitudes which is shown in Fig. 9. The present analysis demonstrates that the disregistry distributions associated with the disconnections and the Type II-1 twin dislocations play a significant role in the transformation CRSS levels. The glide of Type II-1 twinning dislocations which accommodate a significant portion of the misfit strain as well as promoting the lattice rotation is necessary for generation of the habit plane geometry in NiTi. Recently, motivated by the compatibility conditions of the two phases [64,65], Sittner et al. [34,35] have addressed that plastic deformation gradients may arise in the neighboring austenite phase during the transformation front glide. This surmise complies with the findings of the present work and explain the degradation of the functional performance [66,67]. To this end, further research is necessary on the role of habit plane defect structure in stress and thermal hysteresis of shape memory alloys. Meanwhile the effects of strain rate and temperature on the CRSS for transformation are beyond the scope of the present analysis, the calculated theoretical CRSS levels in the present work can be employed as the athermal component of the lattice resistance against the austenite to martensite phase transformation in case thermally activated processes are dominant [68,69]. As the temperature and the local stress state is assumed to govern this transformation path [56,70], with an accurate description of the first and second neighbor interatomic interactions along with the local stress state derived based on the interfacial defect structure at finite temperature, the anisotropic variation of CRSS levels as well as the transformation window can be predicted in NiTi shape memory alloys [68,69,71−73].

5. Conclusions

The following conclusions can be drawn from the present work:

(i) The CRSS values for transformation are calculated by employing the defect structures of the austenite-martensite interface under varying tension loading directions. The resulting CRSS values are shown to be in close agreement with the experimental measurements and exhibit a variation which extends 160 MPa (or nearly a factor of 1.7 change in CRSS).

(ii) Within the framework of topological model, {0.85 0.45 0.27} family habit planes are shown to be generated by the rotation of the {110} terrace planes. The Burgers vectors of interface disconnections and Type II-1 twinning dislocations are calculated to be as <0.25 0.25 0.54 > and $1/9[011]_M$ respectively. The average spacing of both defects which accommodate misfit strains, are calculated to be 11.5 Å.

(iii) The non-Schmid response of NiTi shape memory alloy reflected by anisotropic transformation CRSS levels are evaluated to be closely linked with the short-range interaction between the interfacial defect core and applied loading. The wider defect cores are calculated to decrease the forward transformation CRSS levels.

Acknowledgements

Appendix A

CRSS	Critical Resolved Shear Stress
GSFE	Generalized Stacking Fault Energy
GPFE	Generalized Planar Fault Energy
A	Austenite phase
M	Martensite phase
TP	Terrace plane
a_0	Lattice constant in B2 ordered cubic austenite phase
a, b, c	Lattice constants in B19′ ordered monoclinic martensite phase
β	The angle between the translational symmetry directions with the constants of a and c
Q	Coordinate transformation matrix from monoclinic skeletal lattice to austenite frame
A	Orthogonal rotation matrix in austenite phase
M	Coordinate transformation matrix from monoclinic to austenite coordinate frame
$e_1 - e_2 - e_3$	Terrace plane coordinate frame
h	Interfacial disconnection step height
b^D	Disconnection Burgers vector
ξ^D	Disconnection unit line vector
b^{LIS}	Type II-1 twinning dislocation Burgers vector
ξ^{LIS}	Type II-1 twinning dislocation unit line vector
d^D	Spacing between the interfacial disconnections
d^{LIS}	Spacing between the interfacial twinning dislocations
$\varepsilon_{11}, \varepsilon_{22}$	Misfit strain components in terrace plane coordinate frame
p	The unit normal to the terrace plane
p′	The unit normal of the rotated terrace plane
n	The unit normal to the habit plane
N	The unit normal to Type II-1 twinning plane
R	Net rotation tensor corresponding to the terrace plane
R_1	Rotation tensor associated with the disconnections
ω_1	Unit vector along the rotation axis of R_1
ψ_1	The angle of rotation about ω_1
R_2	Rotation tensor associated with the twinning dislocations
ω_2	Unit vector along the rotation axis of R_2
ψ_2	The angle rotation about ω_2
$\in$	Third order permutation tensor
b_1, b_2	The Burgers vectors formed by dissociation of b^D
b	Generical Burgers vector
σ_{ij}^∞	The externally applied stress field components
$\sigma_{ij}^1, \sigma_{ij}^2, \sigma_{ij}^{LIS}$	The local stress fields associated with the Burgers vectors of b_1, b_2, b_3
u	Elastic displacement field vector
m	Generic line vector of the disconnection/dislocation
x	Position vector
C_{ijkl}^A	The fourth order elastic stiffness tensor of austenite phase
C_{ijkl}^M	The fourth order elastic stiffness tensor of martensite phase
S_{ijkl}	The fourth order elastic compliance tensor
$p_\alpha^A, A_{i\alpha}^A, E_\alpha^A, L_{i\alpha}^A$	Complex constants of Eshelby-Stroh formalism in austenite phase
$p_\alpha^M, A_{i\alpha}^M, E_\alpha^M, L_{i\alpha}^M$	Complex constants of Eshelby-Stroh formalism in martensite phase
$\kappa_1, \kappa_2, \kappa_{LIS}$	Stress field expressions related to $\sigma_{ij}^1, \sigma_{ij}^2, \sigma_{ij}^{LIS}$
$\phi_1, \phi_2, \phi_{LIS}$	Stress field expressions related to $\sigma_{ij}^1, \sigma_{ij}^2, \sigma_{ij}^{LIS}$
E^{tot}	Total energy functional
E^{trans}	Transformation energy
E^e	Elastic strain energy
E^{twin}	Short range atomic misfit energy of Type II-1 twinning

E^{mis}	The net short range atomic misfit energy of disconnection
E_1	The misfit energy associated with b_1
E_2	The misfit energy associated with b_2
W	The net work applied on the disconnections and Type II-1 twinning dislocations
γ_1, γ_2	The GSFE profile variables along b_1 and b_2
γ_3	The GPFE profile variable along b^{LIS}
f	Disregistry field
c_i, ζ_i	Core width parameters
u	Total transformation displacement
s, v, t	Parametric coordinates along b_1, b_2 and b^{LIS} vectors
s_1, v_2, t_3	Centroids of the f_1, f_2 and f_3 disregistry fields
S, V, T	Unit tangent vectors along b_1, b_2 and b^{LIS} vectors
ρ	Infinitesimal dislocation density field
d_1, d_2, d_3	The distance of translational symmetry along b_1, b_2 and b^{LIS}
Λ	Geometrical projection factor

Appendix B. Supplementary data

Supplementary data to this article can be found online at https://doi.org/10.1016/j.actamat.2019.06.009.

References

[1] S. Alkan, A. Ojha, H. Sehitoglu, The complexity of non-Schmid behavior in the CuZnAl shape memory alloy, J. Mech. Phys. Solids 114 (2018) 238–257.
[2] S. Alkan, H. Sehitoglu, Non-Schmid response of Fe3Al: the twin-antitwin slip asymmetry and non-glide shear stress effects, Acta Mater. 125 (2017) 550–566.
[3] H. Sehitoglu, S. Alkan, Recent progress on modeling slip deformation in shape memory alloys, Shape Mem. Superelasticity 4 (2018) 11–25.
[4] S. Alkan, H. Sehitoglu, Plastic flow resistance of NiTiCu shape memory alloy-theory and experiments, Acta Mater. 163 (2019) 173–188.
[5] S. Alkan, H. Sehitoglu, Dislocation core effects on slip response of NiTi- a key to understanding shape memory, Int. J. Plast. 97 (2017) 126–144.
[6] H. Sehitoglu, J. Jun, X. Zhang, I. Karaman, Y. Chumlyakov, H.J. Maier, K. Gall, Shape memory and pseudoelastic behavior of 51.5%Ni–Ti single crystals in solutionized and overaged state, Acta Mater. 49 (2001) 3609–3620.
[7] K.A. Gall, The Effect of Stress State and Precipitation on Stress-Induced Martensitic Transformations in Polycrystalline and Single Crystal Shape Memory Alloys: Experiments and Micro-mechanical Modeling. Mechanical Engineering, Dissertation, University of Illinois at Urbana-Champaign, 1998.
[8] N.S. Surikova, Y.I. Chumlyakov, Mechanisms of plastic deformation of the titanium nickelide single crystals, Phys. Met. Metallogr. 89 (2000) 196.
[9] K. Gall, H. Sehitoglu, Y.I. Chumlyakov, I.V. Kireeva, Tension–compression asymmetry of the stress–strain response in aged single crystal and polycrystalline NiTi, Acta Mater. 47 (1999) 1203–1217.
[10] J.P. Hirth, The influence of grain boundaries on mechanical properties, Metall. Trans. 3 (1972) 3047–3067.
[11] A.P. Sutton, R.W. Balluffi, Interfaces in Crystalline Materials, Clarendon Press, 1995.
[12] E. Arzt, M.F. Ashby, R.A. Verrall, Interface controlled diffusional creep, Acta Metall. 31 (1983) 1977–1989.
[13] K.T. Aust, U. Erb, G. Palumbo, Interface control for resistance to intergranular cracking, Mater. Sci. Eng. A 176 (1994) 329–334.
[14] X. Zhou, X.Y. Li, K. Lu, Enhanced thermal stability of nanograined metals below a critical grain size, Science 360 (2018) 526.
[15] C.C. Koch, Structural nanocrystalline materials: an overview, J. Mater. Sci. 42 (2007) 1403–1414.
[16] W.J. Lu, R.S. Qin, Influence of κ-carbide interface structure on the formability of lightweight steels, Mater. Des. 104 (2016) 211–216.
[17] T.H. Chen, K.L. Weng, J.R. Yang, The effect of high-temperature exposure on the microstructural stability and toughness property in a 2205 duplex stainless steel, Mater. Sci. Eng. A 338 (2002) 259–270.
[18] W.T. Read, W. Shockley, Dislocation models of crystal grain boundaries, Phys. Rev. 78 (1950) 275–289.
[19] F.C. Frank, Symposium on the plastic deformation of crystalline solids, in: Symposium on the Plastic Deformation of Crystalline Solids. Pittsburgh: Office of Naval Research, 1950, p. 150.
[20] B.A. Bilby, Report on the conference on defects in crystalline solids, in: Report on the Conference on Defects in Crystalline Solids. London: the Physical Society, 1955.
[21] R.W. Balluffi, Y. Komem, T. Schober, Electron microscope studies of grain boundary dislocation behavior, Surf. Sci. 31 (1972) 68–103.
[22] H.I. Aaronson, Observations on interphase boundary structure, J. Microsc. 102 (1974) 275–300.
[23] W. Bollmann, Crystal Defects and Crystalline Interfaces, Springer-Verlag, 1970.
[24] K.M. Knowles, The dislocation geometry of interphase boundaries, Philos. Mag. A 46 (1982) 951–969.
[25] A.J. Vattré, M.J. Demkowicz, Determining the Burgers vectors and elastic strain energies of interface dislocation arrays using anisotropic elasticity theory, Acta Mater. 61 (2013) 5172–5187.
[26] R.C. Pond, Interfacial dislocations, in: F.R.N. Nabarro (Ed.), Dislocations in Solids, vol. 8, Elsevier, Amsterdam, 1989.
[27] R.C. Pond, J.P. Hirth, Defects at surfaces and interfaces, in: H. Ehrenreich, D. Turnbull (Eds.), Solid State Physics, vol. 47, Academic Press, 1994, pp. 287–365.
[28] J.P. Hirth, R.C. Pond, R.G. Hoagland, X.Y. Liu, J. Wang, Interface defects, reference spaces and the Frank–Bilby equation, Prog. Mater. Sci. 58 (2013) 749–823.
[29] F. Dalle, E. Perrin, P. Vermaut, M. Masse, R. Portier, Interface mobility in Ni49.8Ti42.2Hf8 shape memory alloy, Acta Mater. 50 (2002) 3557–3565.
[30] R. Sinclair, H.A. Mohamed, Lattice imaging study of a martensite-austenite interface, Acta Metall. 26 (1978) 623–628.
[31] J. Wang, H. Sehitoglu, H.J. Maier, Dislocation slip stress prediction in shape memory alloys, Int. J. Plast. 54 (2014) 247–266.
[32] T. Ezaz, J. Wang, H. Sehitoglu, H.J. Maier, Plastic deformation of NiTi shape memory alloys, Acta Mater. 61 (2013) 67–78.
[33] R.F. Hamilton, H. Sehitoglu, Y. Chumlyakov, H.J. Maier, Stress dependence of the hysteresis in single crystal NiTi alloys, Acta Mater. 52 (2004) 3383–3402.
[34] L. Heller, H. Seiner, P. Šittner, P. Sedlák, O. Tyc, L. Kadeřávek, On the plastic deformation accompanying cyclic martensitic transformation in thermomechanically loaded NiTi, Int. J. Plast. 111 (2018) 53–71.
[35] P. Šittner, P. Sedlák, H. Seiner, P. Sedmák, J. Pilch, R. Delville, L. Heller, L. Kadeřávek, On the coupling between martensitic transformation and plasticity in NiTi: experiments and continuum based modelling, Prog. Mater. Sci. 98 (2018) 249–298.
[36] S. Miyazaki, S. Kimura, F. Takei, T. Miura, K. Otsuka, Y. Suzuki, Shape memory effect and pseudoelasticity in a Ti-Ni single crystal, Scripta Metall. 17 (1983) 1057–1062.
[37] Y. Liu, Z.L. Xie, J. Van Humbeeck, L. Delaey, Effect of texture orientation on the martensite deformation of NiTi shape memory alloy sheet, Acta Mater. 47 (1999) 645–660.
[38] J. Wang, Z. Moumni, W. Zhang, A thermomechanically coupled finite-strain constitutive model for cyclic pseudoelasticity of polycrystalline shape memory alloys, Int. J. Plast. 97 (2017) 194–221.
[39] H.I. Aaronson, T. Furuhara, J.M. Rigsbee, W.T. Reynolds, J.M. Howe, Crystallographic and mechanistic aspects of growth by shear and by diffusional processes, Metall. Trans. A 21 (1990) 2369–2409.
[40] J.W. Christian, Deformation by moving interfaces, Metall. Trans. A 13 (1982) 509–538.
[41] A.N. Stroh, Dislocations and cracks in anisotropic elasticity, Phil. Mag. 3 (1958) 625–646.
[42] R.C. Pond, T. Nixon, Defect modelling of martensitic transformations in NiTi, Mater. Sci. Forum 327–328 (2000) 139.
[43] S. Plimpton, Fast parallel algorithms for short-range molecular dynamics, J. Comput. Phys. 117 (1995) 1–19.
[44] G. Ren, H. Sehitoglu, Interatomic potential for the NiTi alloy and its application, Comput. Mater. Sci. 123 (2016) 19–25.
[45] M. Dupeux, R. Bonnet, Stresses, displacements and energy calculations for interfacial dislocations in anisotropic two-phase media, Acta Metall. 28 (1980) 721–728.
[46] D.M. Barnett, J. Lothe, An image force theorem for dislocations in anisotropic bicrystals, J. Phys. F Met. Phys. 4 (1974) 1618.
[47] J.D. Eshelby, W.T. Read, W. Shockley, Anisotropic elasticity with applications to dislocation theory, Acta Metall. 1 (1953) 251–259.
[48] S. Alkan, H. Sehitoglu, Dislocation core effects on slip response of NiTi- a key to understanding shape memory, Int. J. Plast. 97 (2017) 126–144.
[49] K. Otsuka, T. Sawamura, K. Shimizu, Crystal structure and internal defects of equiatomic TiNi martensite, Phys. Status Solidi 5 (1971) 457–470.
[50] K.M. Knowles, D.A. Smith, The crystallography of the martensitic transformation in equiatomic nickel-titanium, Acta Metall. 29 (1981) 101–110.
[51] Z.L. Xie, Y. Liu, HRTEM study of <011> type II twin in NiTi shape memory alloy, Phil. Mag. 84 (2004) 3497–3507.
[52] T. Ezaz, H. Sehitoglu, Type II detwinning in NiTi, Appl. Phys. Lett. 98 (2011) 141906.
[53] O. Matsumoto, S. Miyazaki, K. Otsuka, H. Tamura, Crystallography of martensitic transformation in Ti-Ni single crystals, Acta Metall. 35 (1987) 2137–2144.
[54] R.C. Pond, S. Celotto, J.P. Hirth, A comparison of the phenomenological theory of martensitic transformations with a model based on interfacial defects, Acta Mater. 51 (2003) 5385–5398.
[55] M.-X. Zhang, P.M. Kelly, Crystallographic features of phase transformations in solids, Prog. Mater. Sci. 54 (2009) 1101–1170.
[56] J. Wang, H. Sehitoglu, Resolving quandaries surrounding NiTi, Appl. Phys. Lett. 101 (2012), 081907.
[57] V. Vitek, Theory of the core structures of dislocations in body-centred-cubic metals, Cryst. Lattice Defects 5 (1974) 1–34.
[58] J. Eshelby, LXXXII, Edge dislocations in anisotropic materials, London,

Edinburgh, Dublin Philosoph. Mag. J. Sci. 40 (1949) 903–912.

[59] K. Gall, H. Sehitoglu, The role of texture in tension-compression asymmetry in polycrystalline NiTi, Int. J. Plast. 15 (1999) 69–92.

[60] S. Alkan, Y. Wu, H. Sehitoglu, Giant non-Schmid effect in NiTi, Extreme Mech. Lett. 15 (2017) 38–43.

[61] A.J. Bogers, W.G. Burgers, Partial dislocations on the {110} planes in the B.C.C. lattice and the transition of the F.C.C. into the B.C.C. lattice, Acta Metall. 12 (1964) 255–261.

[62] A. Ojha, H. Sehitoglu, Transformation stress modeling in new FeMnAlNi shape memory alloy, Int. J. Plast. 86 (2016) 93–111.

[63] X.-S. Yang, S. Sun, X.-L. Wu, E. Ma, T.-Y. Zhang, Dissecting the mechanism of martensitic transformation via atomic-scale observations, Sci. Rep. 4 (2014) 6141.

[64] J.M. Ball, R.D. James, Fine phase mixtures as minimizers of energy, Arch. Ration. Mech. Anal. 100 (1987) 13–52.

[65] J.M. Ball, C. Carstensen, Compatibility conditions for microstructures and the austenite–martensite transition, Mater. Sci. Eng. A 273–275 (1999) 231–236.

[66] S. Miyazaki, T. Imai, Y. Igo, K. Otsuka, Effect of cyclic deformation on the pseudoelasticity characteristics of Ti-Ni alloys, Metall. Trans. A 17 (1986) 115–120.

[67] S. Miyazaki, My experience with Ti–Ni-based and Ti-based shape memory alloys, Shape Mem. and Superelasticity 3 (2017) 279–314.

[68] G. Ghosh, G.B. Olson, Kinetics of F.c.c. → b.c.c. heterogeneous martensitic nucleation—II. Thermal activation, Acta Metall. Mater. 42 (1994) 3371–3379.

[69] G.B. Olson, M. Cohen, A general mechanism of martensitic nucleation: Part III. Kinetics of martensitic nucleation, Metall. Trans. A 7 (1976) 1915–1923.

[70] N. Hatcher, O.Y. Kontsevoi, A.J. Freeman, Role of elastic and shear stabilities in the martensitic transformation path of NiTi, Phys. Rev. B 80 (2009) 144203.

[71] G. Ghosh, V. Raghavan, The kinetics of isothermal martensitic transformation in an Fe-23.2wt.%Ni-2.8wt.%Mn alloy, Mater. Sci. Eng. 80 (1986) 65–74.

[72] U.F. Kocks, A.S. Argon, M.F. Ashby, Thermodynamics and Kinetics of Slip, Pergamon Press, 1975.

[73] C.L. Magee, The kinetics of martensite formation in small particles, Metall. Trans. 2 (1971) 2419–2430.